Peer-reviewed version available at *Nanomaterials* **2018**, *8*, 525; doi:10.3390/nano8070525

Article

Percolated Si:SiO_2 Nanocomposites: Oven- vs. Millisecond Laser-induced Crystallization of SiO_x Thin Films

Erik Schumann [1], René Hübner [1], Jörg Grenzer[1], Sibylle Gemming[1,2], and Matthias Krause [1,*]

[1] Helmholtz-Zentrum Dresden - Rossendorf, Institute of Ion Beam Physics and Materials Research, Bautzner Landstraße 400, 01328 Dresden, Germany; matthias.krause@hzdr.de
[2] Institute of Physics, Technische Universität Chemnitz, 09107 Chemnitz, Germany
* Correspondence: matthias.krause@hzdr.de; Tel.: +49-351-260-3578

Abstract: Three-dimensional nanocomposite networks consisting of percolated Si nanowires in a SiO_2 matrix, Si:SiO_2, were studied. The structures were obtained by reactive ion beam sputter deposition of SiO_x (x≈0.6) thin films at 450°C and subsequent crystallization using conventional oven as well as millisecond line focus laser annealing. Rutherford backscattering spectrometry, Raman spectroscopy, X-ray diffraction, cross-sectional and energy-filtered transmission electron microscopy were applied for sample characterization. While oven annealing resulted in a mean Si wire diameter of 10 nm and a crystallinity of 72 % within the Si volume, almost single-domain Si structures with 30 nm in diameter and almost free of amorphous Si were obtained by millisecond laser application. The structural differences are attributed to the different crystallization processes: Conventional oven tempering proceeds via solid state, millisecond laser application via liquid phase crystallization of Si. The 5 orders of magnitude larger diffusion constant in the liquid phase is responsible for the three times larger Si nanostructure diameter. In conclusion, laser annealing offers not only significantly shorter process times but moreover a superior structural order of nano-Si compared to conventional heating.

Keywords: silicon; nanostructures; percolated networks; nanocomposites; thin films; laser processing; phase separation; liquid phase crystallization

1. Introduction

Since the introduction of the first transistor[1–3] silicon-based technology has determined the technological progress in the world significantly and it has changed the way of life of our society in many areas. Despite great progress and expectations raised by other materials, silicon is still the material of choice for the further development of key technologies like nanoelectronics, photovoltaics, light emitting or energy storage[4,5]. Silicon is the second most abundant element in the earth crust and hence, has the potential to promote a sustainable technology progress.

Silicon nanostructures can be based on spherical / dot-like or cylindrical / wire-like geometries. Nanodots are usually supported by an insulating silicon dioxide matrix which constrains electrical conduction[6]. Wire-like nanostructures on the other hand are usually not supported by an additional matrix[4]. However, when they are in direct contact with air, oxidation leads to a few nm thin native oxide layer and additional near-surface defects are formed, lowering the electrical performance of these structures.

An alternative approach to obtain nm-sized Si structures is the formation of a nanocomposite of percolated Si in a SiO_2 matrix. As first proposed by kinetic Monte Carlo simulations [7,8], such structures should be formed if a Si-rich oxide, SiO_x, undergoes a phase separation into Si and SiO_2 on the nanometer scale, following equation (1):

$$SiO_x \rightarrow \frac{x}{2} SiO_2 + \left(1 - \frac{x}{2}\right) Si. \quad (1)$$

Peer-reviewed version available at Nanomaterials 2018, 8, 525; doi:10.3390/nano8070525

According to the simulations, the Si nanostructures would be interconnected and expected to exhibit electrical conductivity in a regime of $x \leq 1.1$. Furthermore, these structures should exhibit the advantage of tunable band gap due to quantum confinement[9]. Müller *et al.* [7] experimentally validated percolated Si:SiO_2 nanocomposites by forming a Si-rich oxide via implantation of Si ions into a thin SiO_2 layer. Friedrich *et al.* [10] and Ilday *et al.* [11] used physical vapour deposition to obtain $SiO_{x\approx1}$. Chemical vapour deposition was used by Gundogdu *et al.* [12] for $SiO_{0.8}$ layer fabrication.

Up to now, the as-prepared silicon oxide thin films were processed in an oven, via rapid thermal processing [10,11] at temperatures of 950 °C to 1150 °C for 0.5 min to 60 min or by a point-focus laser beam. After the thermal treatment, the predicted interconnectivity was found[10,11], and even quantum confinement was observed [11]. However, when working with temperature-sensitive substrates or layer structures, only a low-temperature or a very short high-temperature process step can be used for thermal processing in order to keep both unaffected. Such temperature restrictions exist for example in thin film solar cells by the choice of the substrate (float glass, foil). Many industrial applications require to process large areas, in short time with limited heat exposure of the substrate material. So far, these demands have not been fulfilled for percolated Si:SiO_2 nanocomposites. Moreover, primarily the existence of percolated Si in SiO_2 was proven, while the investigation of structural properties like compositional homogeneity, degree of Si crystallinity, Si grain size and strain determination remained open.

A smart technological solution to tackle above-mentioned requirements is line-focus laser processing. Thereby, a mono-energetic beam of coherent light is scanned across the material. This induces heat for a very short time by absorption of light in a defined depth of a thin film, leaving the substrate comparably cold. Beyond depth selectivity and substrate protection, a line-focused diode laser beam enables a homogeneous treatment of a full sample. Line-focused laser processing has not been reported so far for the thermal treatment of SiO_x thin films or for the fabrication of Si nanostructures.

In this work, millisecond line-focus laser treatment was applied to $SiO_{0.6}$ thin films, deposited by ion beam sputter deposition on fused silica. The obtained nanostructures were compared to those formed by conventional oven treatment. Rutherford backscattering spectrometry (RBS), Raman spectroscopy, X-Ray diffraction (XRD) and cross-sectional transmission electron microscopy (TEM) were applied for comprehensive compositional and structural sample characterization after deposition and thermal treatment. As-deposited films have perfect lateral and depth homogeneity. Experimental evidence for phase separation into amorphous Si (a-Si) and SiO_2 prior to thermal treatment is presented. Apart of minor Si enrichment at the surface and the interface to SiO_2, the homogeneous sample composition is conserved during thermal treatments. The oven-treatment resulted in Si:SiO_2 nanocomposites whose Si volume fraction has 72 % crystallinity and a mean Si diameter of about 10 nm. The Si volume fraction obtained by millisecond laser annealing was characterized by more than 90 % crystallinity and almost single domain nano-crystals with about 30 nm mean diameter. The observed structural differences are explained by different diffusion constants for solid and liquid state of matter.

2. Results

Lateral and depth composition of as-deposited, oven-treated and laser-treated $SiO_{0.6}$ were studied by RBS (figure 1). The energy of backscattered He ions is determined by a kinematic factor [13,14]. The heavier the target atoms, the smaller the energy loss of the scattered ion, and the higher the measured backscattering energy. Moreover, the energy loss of the scattered ions is proportional to the depth of the scattering event due to electronic stopping [13,14] and thus, the larger the thickness the smaller the measured scattering energy. The RBS intensity is proportional to the concentration of the elements in a sample. The width of an element-specific signal plateau indicates the thickness of an individual layer.

The RBS spectra of the three studied samples show the following major features: I) the Si signal of the $SiO_{0.6}$ layer at backscattering energies from 970 keV to about 700 keV, II) the Si signal from the

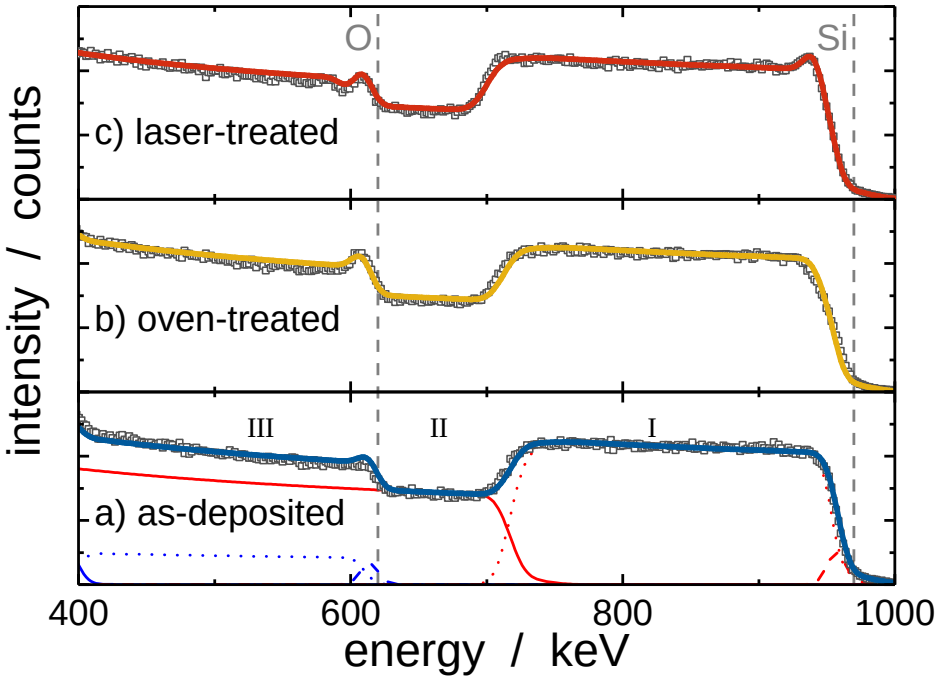

Figure 1. RBS spectra of $SiO_{0.6}$ layers on SiO_2: as-deposited (a), after conventional oven (b), and laser treatment (c). The energy range between 1 keV and 1.7 keV, which shows traces of Ar and W, was omitted for clarity. Squares represent measured data and lines fitted curves. In (a) single layer elemental profiles are shown additinally, i.e. red for Si and blue for O. The roman letters (I, II, III) indicate the major RBS feature types explained in the text.

SiO_2 substrate starting from about 700 keV, and III) the O signal of the $SiO_{0.6}$ from 610 keV to lower energies.

Moreover, all 3 spectra have a peak at the edge of the $SiO_{0.6}$ oxygen signal in common that is attributed to a thin intentionally deposited protective SiO_2 top layer. Complementarily, a flattened Si edge at 970 keV is observed accounting for the reduced Si content in this surface layer compared to the $SiO_{0.6}$ film. Correspondingly, a three-layer stack consisting of SiO_2 surface layer, $SiO_{0.6}$ bulk and SiO_2 substrate is necessary for fitting the main RBS features. Minor constituents, such as tungsten or argon, which originate from the deposition process, represent less than 0.1 % of the sample composition. An overview of the obtained compositions and areal densities derived from the RBS measurements are given in table 1. To correlate areal densities with thicknesses, TEM and SE measurements were conducted, whose data are also presented in table 1.

The lateral composition, that was checked at five 1 mm^2 large areas of the initial 20 mm × 20 mm as-deposited sample was found to be the same within experimental accuracy. A measurement uncertainty of 2 % for the total areal density and the areal density of the elemental Si results in an uncertainty for x of ± 0.06. Across the whole as-deposited sample a thickness variation of 10 % was observed. From the perfect agreement of the RBS data and the corresponding three-layer fit model follows that the elemental depth distribution within the as-deposited and the oven-treated sample is homogeneous.

The RBS spectrum of the laser-treated sample shows an additional peak at the high-energy edge of the $SiO_{0.6}$ bulk signals. This observation requires the introduction of an additional Si-rich intermediate layer between the SiO_2 surface and the $SiO_{0.6}$ bulk, termed as intermediate 1 (table 1). In a similar way, a steeper slope at the low-energy edge of the $SiO_{0.6}$ bulk Si signal is attributed to another Si-rich intermediate layer on its bottom (table 1, intermediate 2).

Total areal densities per element of all three samples agree very well within the experimental accuracy and sample homogeneity, i.e. no loss in material was observed after thermal treatment. Layer

thicknesses obtained by TEM and SE agree within experimental accuracy (5 %) and sample thickness homogeneity (10 %).

Table 1. Overview of RBS results of $SiO_{0.6}$ layers on SiO_2, as-deposited, oven- and laser-treated. Atomic fraction (at. %), areal density (ρ_{area}) of silicon and oxygen, the resulting x of SiO_x fraction and thickness obtained by TEM, d_{TEM}, as well as spectroscopic ellipsometry, d_{SE}, for individual layers observed.

sample	Si		O			TEM thickness	SE thickness
	at. %	ρ_{area} / 10^{15} $\frac{1}{cm^2}$	at. %	ρ_{area} / 10^{15} $\frac{1}{cm^2}$	x of SiO_x	d_{TEM} / nm	d_{SE} / nm
as-deposited							
surface	33.3	33.3	66.6	66.5	2	14	15
bulk	61.0	1691	38.9	1079	0.64	500	509
oven-treated							
surface	33.3	50	66.6	99.8	2	39	40
bulk	60.5	1663	39.4	1084	0.65	501	482
laser-treated							
surface	33.3	50	66.6	99.8	2	28	29
intermediate 1	90.0	90	9.9	9.9	0.11	27	24
bulk	61.5	1648	38.4	1031	0.63	479	446
intermediate 2	90	45	10	5	0.11	24	10.7

Based on the fit models, precise numbers for the atomic compositions of the three-film stacks were derived (table 1). The $SiO_{0.6}$ bulk layer of the as-deposited sample contains about 38.9 % atomic oxygen, corresponding to $SiO_{0.64}$ with an areal density of $2770 \times 10^{15}\,cm^{-2}$. Compared to the as-deposited sample, the oven-annealed $SiO_{0.6}$ film does not show a significant change in bulk composition. The fitted bulk O content of 39.4 % conforms to the bulk O content of the as-deposited layer within the accuracy of measurement and homogeneity of sample deposition, resulting in $SiO_{0.65}$. The surface oxygen peak increases after oven treatment. The protective SiO_2 surface layer apparently grew in thickness to $150 \times 10^{15}\,cm^{-2}$ during the oven treatment, i.e. by about 50 %. Also the laser-treated silicon oxide film does not show a change in the bulk composition (table 1). Its O content of 38.4 %, resulting in $SiO_{0.63}$, is the same as for the other two films within the experimental accuracy. As mentioned before, the oxygen peak superimposed to the high-energy edge of the $SiO_{0.6}$ bulk layer is stronger than in the as-deposited and oven-treated one. Moreover, a peak at the high-energy edge of the $SiO_{0.6}$ Si signal is unambiguously apparent (figure 1). At the same time, a minimum is seen next to the oxygen peak towards lower energy. Both features are described by a thin Si-rich layer, referred to as intermediate 1, underneath the protective SiO_2 surface layer with an areal density of $100 \times 10^{15}\,cm^{-2}$ and a low O content of 10 %. To improve fitting of the low-energy slope of the $SiO_{0.6}$ layer Si signal, an additional Si-rich second intermediate layer with an areal density of $50 \times 10^{15}\,cm^{-2}$ and an oxygen content of 10 % is introduced between the bulk $SiO_{0.6}$ and the silica substrate. This analysis indicates that contrary to oven treatment, laser processing leads to the formation of Si-rich interlayers at both interfaces of the $SiO_{0.6}$ bulk layer.

Raman spectroscopy and X-Ray diffraction are complementary methods for the analysis of phase and micro-structure, lattice strain and crystal size effects in silicon[15,16]. The Raman spectra of as-deposited, oven- and laser-treated $SiO_{0.6}$ show distinct differences in the range from $400\,cm^{-1}$ to $600\,cm^{-1}$, where the F_{2g} crystal vibration and the broad line of a-Si are observed[17–21] (figure 2).

Prior to thermal processing, the observed spectrum shows only one broad line (Full width at half maximum (FWHM $\approx 100\,cm^{-1}$)) with the peak maximum at $485\,cm^{-1}$. It corresponds to that of a-Si[19,22] and indicates a phase separation of $SiO_{0.6}$ into a-Si and SiO_2 occurring already during the

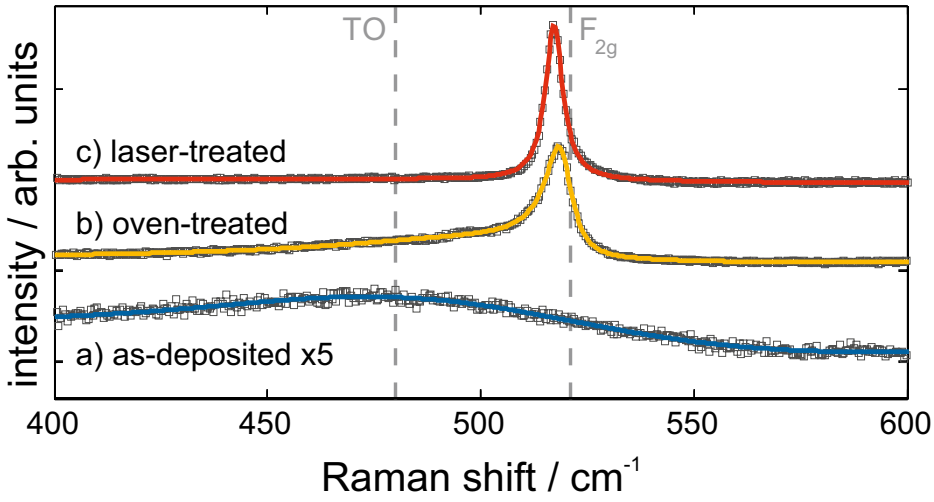

Figure 2. Raman spectra of $SiO_{0.6}$ layers on SiO_2: as-deposited (a), after conventional oven (b), and laser treatment (c). Grey squares represent measured spectral data points and solid lines fitted spectra. Dashed lines indicate the expected positions of the TO-like band associated with a-Si and the F_{2g} phonon mode of c-Si.

deposition and not only after high-temperature processing as predicted and reported in the literature for this material system. After oven tempering, the spectrum comprises a sharp strong line at slightly less than 521 cm^{-1} with an extended low-energy shoulder. Fitting this Raman spectrum with one Breit-Wigner function (BWF, asymmetry factor q = −7.2) and two Gaussians gives line positions (relative integral intensities) of 519 cm^{-1} (60 %), 500 cm^{-1} (6 %) and 482 cm^{-1} (34 %). This is the typical Raman signature of so-called micro-crystalline silicon, consisting of nanocrystalline and amorphous Si fractions[23,24]. The sharp peak at 519 cm^{-1} is attributed to the F_{2g} phonon mode of the nanocrystalline silicon fraction (c-Si). Its FWHM of 7.9 cm^{-1} is two to three times larger than the natural linewidth of single-crystalline silicon at room temperature reported in the literature (≈3.5 cm^{-1})[25,26] or that of a reference Si wafer sample (2.8 cm^{-1}). The shoulder peak with the intensity maximum at 482 cm^{-1} represents the a-Si fraction in the sample, and the intermediate line at 500 cm^{-1} is attributed to Si with wurtzite-type or near surface Si (def-Si)[24,27–29]. Laser treatment of the $SiO_{0.6}$ results in a structure whose Raman spectrum exhibits only one single strong peak at first glance (figure 2). Best line fitting results (r^2 = 0.996) were obtained assuming a BWF (FWHM = 5 cm^{-1}) and Gaussian lines with Raman shifts (relative integral intensities) of 517 cm^{-1} (86 %) and 470 cm^{-1} (14 %).

The crystalline Si volume fraction ρ_c is often estimated from the integral Raman intensities by equation 2[30]:

$$\rho_c = \frac{I_{c-Si} + I_{def-Si}}{I_{c-Si} + I_{def-Si} + yI_{a-Si}} \quad (2)$$

The crystallite-size-dependent integrated Raman cross sections, $y = \sum_{c-Si} / \sum_{a-Si}$, determines the Raman line shape of the crystalline Si[30,31]. Provided that a BWF line shape gives the best fitting results for the c-Si Raman profile, a minimum crystallite size L is L ≥ 15 nm and thus, the minimum y-value of $y = 0.65$, is reported in the literature[30]. On the other hand, this criterion for the estimation of the crystallite size is rather weak, and thus, the mean Si crystallite size has been determined here from X-Ray diffraction and was then used to apply equation 2. Another diagnostic criterion to estimate the Si crystallite size from Raman data consists in the use of the correlation between F_{2g} line widths and crystallite sizes determined by X-Ray diffraction. Comparing our FWHM of 7.9 cm^{-1} and 5.0 cm^{-1} with such a correlation from the literature[16], gives values of approximately 8 nm and > 15 nm for the oven- and laser-treated samples.

Preprints (www.preprints.org) | NOT PEER-REVIEWED | Posted: 4 June 2018 doi:10.20944/preprints201806.0022.v1

Peer-reviewed version available at Nanomaterials 2018, 8, 525; doi:10.3390/nano8070525

None of the three Raman spectra showed any contribution of SiO_2, neither at first glance nor during spectra fitting. Its absence is caused by its low Raman cross section due to the energy gap of the order of 9 eV [32,33].

In figure 3 i) XRD intensities of as-deposited, oven- as well as laser-treated $SiO_{0.6}$ are shown over the scattering vector $Q = \frac{2}{\lambda}\sin(\Theta)$, with λ being the incident beam wavelength and Θ the scattering angle. The subfigures ii) and iii) show Williamson-Hall (WH) plots of the oven- and laser-treated samples. For the as-deposited film, no diffraction peaks were observed. The broad feature

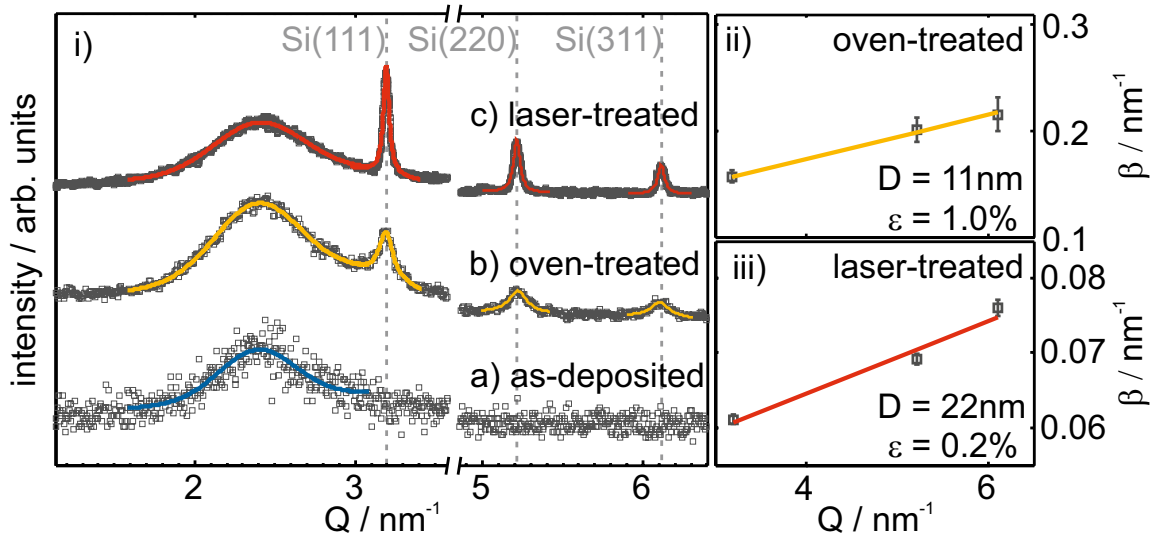

Figure 3. i) XRD patterns of $SiO_{0.6}$ layers on SiO_2: as-deposited (a), after conventional oven (b), and laser treatment (c). The broad peak at about 2.4 nm^{-1} originates from the a-SiO_2 matrix and silica substrate. Measurement data are shown by grey squares. The solid lines represent fitted curves. (ii)+(iii) The determined diffraction peak width is plotted vs. its position, the linear regression was made for Williamson-Hall analysis to retrieve crystallite size D and micro-strain ϵ for the oven- (ii) and laser-treated (iii) sample.

at ≈2.4 nm^{-1}, which is also seen in the other diffraction patterns, originates from the amorphous SiO_2 substrate and matrix. Therefore, the as-deposited film is X-ray-amorphous and does not exhibit a crystalline phase. Oven treatment leads to the evolution of three diffraction peaks at about 3.19 nm^{-1}, 5.22 nm^{-1} and 6.11 nm^{-1} which correspond to the (111), (220) and (311) lattice planes of Si[34]. The observed line widths are broad and show an increase with increasing scattering vector. After laser treatment, diffraction peaks at the same positions are observed, but with higher intensity as well as narrower linewidth. The increased intensity can be correlated with an increased scattering volume of well-ordered lattice planes (i.e. a higher density of crystallites in the layer), and the smaller linewidth results from larger crystallite sizes, compared to the oven-treated sample.

The observed peaks assigned to Si lattice planes were fitted by Lorentzians. From the obtained peak positions and the assigned Miller indices, the mean lattice spacing is calculated to 5.425(7) Å and 5.424(1) Å for the oven- and laser-treated films, respectively. These values differ at most by 0.007 Å or 0.13 % from the literature value of 5.431 Å[34] for the lattice spacing of strain-free silicon. In the subsets of figure 3, the fitted and for instrumental resolution corrected integral width are plotted against the peak positions following the method by Williamson and Hall [35]. From linear regression, the Si crystallite size and the micro strain, the varying of the lattice parameter, ϵ can be calculated following $\beta = 1/D + 2\epsilon Q$. For the oven-treated sample, a crystallite size of 11 nm and a lattice constant variation of 1.0 % are retrieved. After laser processing larger Si crystallites of 22 nm and less a lattice constant variation (0.2 %) are apparent. Together, the obtained mean lattice parameter and Williamson-Hall

analysis of line broadening with increasing scattering vector suggest a slightly compressed Si crystal lattice. This could be a result of vacancies in the Si lattice.

XRR studies (not shown) of as-deposited, oven- and laser-treated samples showed an increase in surface roughness after laser treatment to about 7 nm, whereas the as-deposited and oven-treated sample exhibit a surface roughness of about 3 nm.

Having determined the mean crystallite sizes by XRD, the corresponding values are used to calculate the integrated Raman cross sections, $y = \sum_{c-Si} / \sum_{a-Si}$, for insertion into equation 2. This gives y-values of 0.74 and 0.51, and crystalline Si volume fractions of 72 % and 92 % for the oven- and laser-treated samples, respectively.

While Raman spectroscopy and X-ray diffraction allow structural characterization on an integral scale, TEM reveals details of the microstructure up to atomic resolution in selected, spatially-confined sample regions. High-resolution cross-sectional TEM micrographs (figure 4, a) of the as-deposited $SiO_{0.6}$ layer do not show any hints for crystalline Si. After oven treatment, areas with clearly noticeable

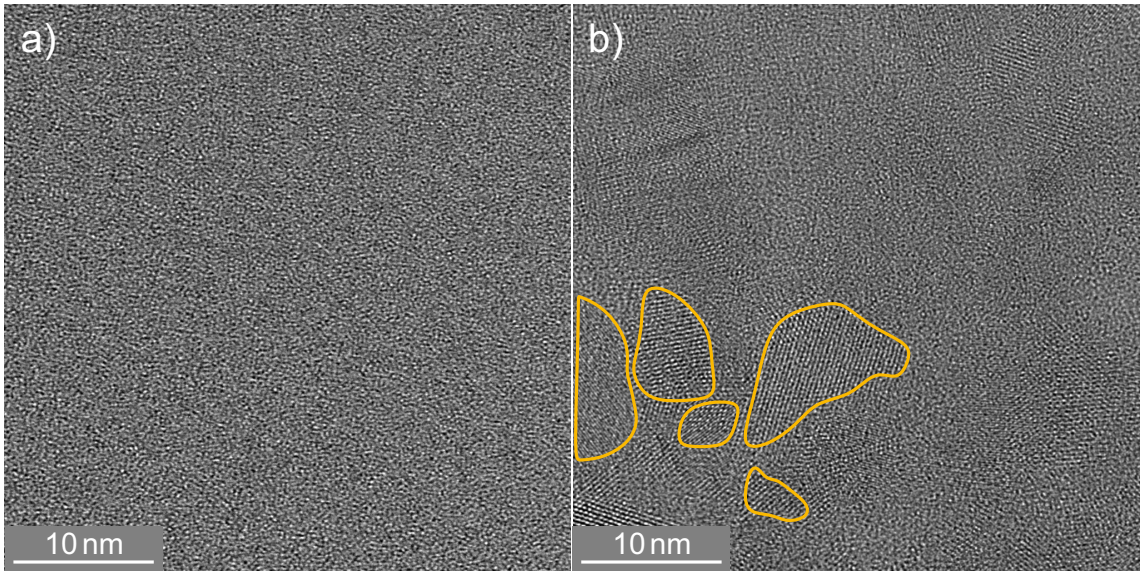

Figure 4. High-resolution TEM image of $SiO_{0.6}$ layers: as-deposited (a) and after conventional oven treatment (b).

lattice fringes are visible, a selection of them is marked in figure 4 b). Lattice planes are randomly oriented and regions with the same orientation have dimensions as large as 12 nm. The TEM lamella thickness is of the order of a few 10 nm and hence much larger than the observed crystallite size. Therefore, one should keep in mind that separated single crystallites might appear to form a connected path, due to the projection of the depth information onto a 2D image.

In figure 5 (a) an image of laser-crystallized $SiO_{0.6}$ is shown. Across the whole field of view, a single orientation of Si lattice planes is visible, i.e. only a single grain and no grain boundaries are seen. The two insets (b+c) depict enlargements of the diagonal corners of a crystalline Si grain. The matrix surrounding this Si crystallite is amorphous SiO_2. An infinitesimally thin a-Si layer at the interface can not be excluded, but is not visible due to the lack of mass contrast between SiO_2 and Si. The distance of 10 distinct lattice planes was measured and yielded approximately 3.1 nm resulting in a mean lattice plane spacing of 3.1 Å. This value agrees with the Si(111) lattice spacing of 3.14 Å[34].

None of the techniques applied so far provides information about the spatial distribution and connection of the individual Si and SiO_2 phases within the thin layer, i.e. about whether a nano-sized percolated structure was formed. Therefore, energy-filtered transmisstion electron microscopy (EFTEM) was used to resolve the spatial distribution of separated Si and SiO_2 (figure 6). For the Si distribution, electrons with an energy loss of 17 eV, due to the excitation of silicon plasmons were used, while the

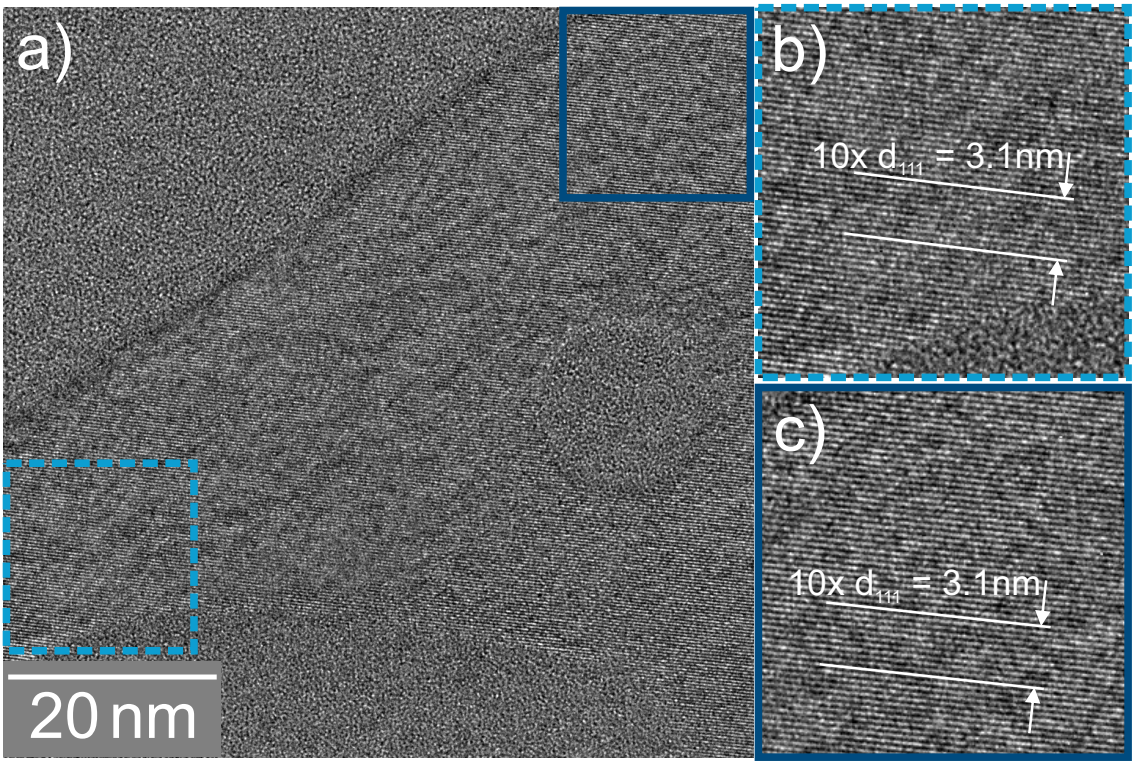

Figure 5. High-resolution TEM image of laser-crystallized $SiO_{0.6}$ layers. (a) Si (111) lattice fringes expand across the whole field of view. The matrix surrounding the crystal is assumed to be SiO_2. (b) and (c) show enlargements of diagonal opposite areas of (a).

complementary SiO_2 distribution (not shown here) was obtained by imaging with electrons which exhibited an energy loss of about 27 eV. Although illuminating the particular region of the TEM lamella only for the EFTEM analysis which was conducted as fast as possible to avoid electron-beam-induced specimen decomposition, the cross-sectional image of as-deposited $SiO_{0.6}$ (figure 6 a) shows distinct image contrast between Si (bright) and SiO_2 nanoparticles (dark). The corresponding Si feature size can be estimated to be about 2 nm. This result confirms the occurrence of phase separation upon deposition. As the structure size is much smaller than the specimen thickness, by EFTEM a conclusion whether a projection of a number of isolated particles or a percolated structure is present cannot be drawn. After oven processing (figure 6 b), the Si plasmon-loss filtered TEM image reveals a coarsend microstructure with a feature size of about 10 nm. Again it is not definite whether the observed Si structures are fully percolated. The laser-processed film (figure 6 c) consists of, compared to oven-treated structures, a similar Si morphology with a much broader size. The measured mean bar width yields 30 nm. Since these structure sizes are comparable to the TEM specimen thickness, the formation of a percolated Si network is unambiguously shown in this case. Friedrich *et al.* [10] and Liedke *et al.* [8] reported percolated Si structures with a mean feature size of 3 nm for Si:SiO_2 systems with a lower Si volume concentration. Based on the EFTEM analysis (figure 6), the higher Si volume fraction compared to Liedke *et al.* [8], Friedrich *et al.* [10], and percolation theory it is deduced that three-dimensional percolated Si structures are present in all $SiO_{0.6}$ thin-films of our study.

3. Discussion

As-deposited, oven- and laser-treated SiO_x films of this study were shown to have the same bulk composition of $SiO_{0.64\pm0.06}$ and to be phase-separated into Si and SiO_2, independently of the sample

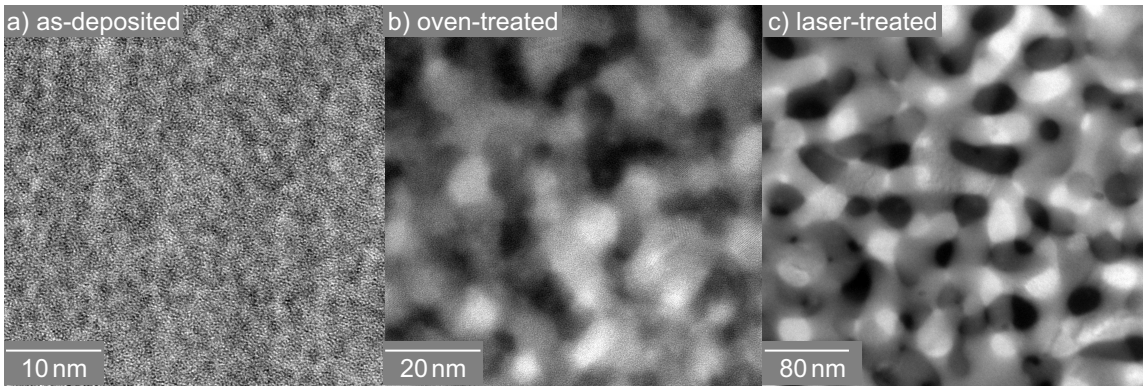

Figure 6. Cross-sectional Si plasmon-loss filtered TEM images (E_{loss}=17 eV) of $SiO_{0.6}$ layers: as-deposited (a), after conventional oven (b), and laser treatment (c).

treatment. The occurrence of phase separation during deposition is independently shown by Raman and EFTEM, in contrast to previous studies of this material system.

Percolated networks of different structure size are formed. By thermal treatment crystallization of a-Si and coarsening of the initial network occurred. In the following, i) the structural properties of the three layer types, ii) the origin of the different structure sizes, and iii) the processes leading to the formation of Si-rich interface layers is discussed.

3.1. Comparison of structural properties

A comparison of the structure properties and treatment parameters is shown in table 2. Oven treatment of the as-deposited, phase-separated Si:SiO_2 structure leads to a coarsening of the

Table 2. Treatment parameters and selected structure properties of as-deposited, oven- or laser-treated $SiO_{0.6}$ layers.

	as-deposited	oven	laser
treatment realization			
exposition time	-	270 min ≡ 16 200 s	17×10^{-3} s
temperature	-	950 °C	n/a
resulting structure properties			
bulk composition	$SiO_{0.64}$	$SiO_{0.65}$	$SiO_{0.63}$
EFTEM structure size	2 nm	10 nm	30 nm
XRD grain size	n/a	11 nm	22 nm
Raman CVF	0 %	72 %	92 %

as-deposited morphology, and to crystallization of the main fraction of the initially amorphous Si. The result is a coexistence of crystalline and a minor fraction of a-Si. The crystallites have random orientation and a mean grain size of 11 nm. XRD analysis yields a lattice parameter variation of about 1 %, with a tendency to smaller values of the lattice constant.

Silicon nanostructures obtained by laser treatment of $SiO_{0.6}$ exhibit a three times larger structure size than those obtained by oven processing. Its crystalline volume fraction is much higher, i.e. almost no amorphous Si phase was observed. Obtained Si crystallites exhibit a mean grain size of 22 nm and are extended for up to 100 nm. The XRD lattice parameter is reduced by 0.2 % compared to a Si powder reference. No signs of crystallized SiO_2 were found for both thermal processing methods.

A decrease of the Raman frequency of the peak associated with crystalline Si is observed for both, oven- (2 cm^{-1}) and laser- (4 cm^{-1}) treated samples. A decrease in the resonance frequency of the collective lattice motion can be caused by phonon confinement or by an increased mean lattice spacing

compared to the reference due to the presence of strain [16,36–40] or by an increased temperature[21]. The grain sizes derived by EFTEM and complementary by XRD analysis yield structure sizes too large for phonon confinement, since for this effect, a typical size below 10 nm has to be reached[4]. Sample heating during Raman measurement were excluded, since no dependence of the applied laser power on the Raman signal was found.

XRD measurements shown above yield a deviation of the mean lattice spacing compared to bulk silicon. The observed deviation of the lattice distance was at most 0.13 % smaller than for the bulk Si literature value, suggesting a compressed silicon lattice. Likewise, Williamson-Hall analysis yielded a lattice parameter variation of the order of 1.0 % for oven- and 0.2 % for laser-treated films. On the other hand, a down-shift of the Raman peak of 2 cm^{-1} to 4 cm^{-1} would suggest an expanded lattice, due to a tensile stress of 1.7 GPa to 3.6 GPa[41,42]. Such stress would lead to a lattice expansion of 0.39 % to 1.38 %. Hence, Raman results seem to contradict the XRD results. But due to the measurement geometries applied, XRD probes the out-of-plane Si lattice distances, whereas Raman in the applied 180° scattering geometry is sensitive to the in-plane Si geometries. During heat treatment, relaxation of stresses at Si-SiO_2 interfaces takes place, which is reduced and eventually inhibited during cooling. The thermal expansion coefficient for the SiO_2 substrate ($\alpha \approx 0.5 \times 10^{-6}\,K^{-1}$[43]) is much smaller than the thermal expansion coefficient for Si ($\alpha \approx 2.6 \times 10^{-6}\,K^{-1}$[44,45]). It follows that the contraction of the Si phase in the thin film is inhibited mainly by the relative lower contraction of the SiO_2 substrate. This in-plane tensile stress results in an in-plane expansion of the lattice. To compensate the in-plane expansion, a compression of the out-of-plane Si lattice components follows.

3.2. Origin of different structure sizes

An objective is to gain insight into the formation processes, leading to Si:SiO_2 nanocomposites. In general, during the thermal treatments, two processes must take place: a) growth of the structure size of the as-deposited nano-network of the Si:SiO_2 nanocomposite and b) crystallization of the Si phase. The initial point is a mixture of as-deposited a-Si and SiO_2 as was observed by Raman as well as by EFTEM measurements. Certainly, a fully phase-separated material with sharp interfaces cannot be assumed after deposition. Most likely, transition regions between the two phases with an amorphous SiO_x exist, where thermal treatment leads to an enhanced phase separation.

Generally, during the growth of the as-deposited Si:SiO_2 nano-composite, diffusion of Si- and/or O- atoms has to take place in the silicon and/or silica phase. Bulk diffusion of Si- and O-atoms in the silica phase is rather low (Si: $1 \times 10^{-19}\,cm^2\,s^{-1}$[46,47]; O: $1 \times 10^{-16}\,cm^2\,s^{-1}$[47]) for the temperature applied during oven treatment. Similarly, Si self-diffusion by self-interstitial or vacancy transport is limited to $1 \times 10^{-17}\,cm^2\,s^{-1}$[47] at 950 °C. The diffusion of O-atoms in silicon by interstitial transport on the other hand, reaches diffusion constants of $1 \times 10^{-11}\,cm^2\,s^{-1}$ at 950 °C, which is 5 orders of magnitude larger than any other regarded diffusion. In addition to bulk diffusion, Si- and O-atoms can diffuse along grain boundaries, which is about 4-8 orders of magnitude faster[48]. Approaching the melting point of a material, the diffusivity of grain boundary diffusion converges to the bulk diffusivity[47]. Hence, the relevant transport for the coarsening of the Si:SiO_2 nanocomposite is the one of O-atoms in the silicon matrix by interstitial transport and the transport of Si- and O-atoms along grain boundaries.

Observed in this work are a considerable smaller structure size and lower crystalline volume fraction after oven treatment compared to laser processing, while the treatment time is 7 orders of magnitude longer. The temperature for oven treatment is 950 °C, whereas the temperature achieved during laser processing is not accessible. The energy input for laser treatment can be estimated as follows. During laser treatment an energy of 110 $J\,cm^{-2}$ is applied to the sample, taking the laser power and dwell time into account. When regarding the absorption of the laser wavelength by the $SiO_{0.6}$ layer 7.2 $J\,cm^{-2}$ are absorbed by the material. In contrast an energy of 210 $J\,cm^{-2}$ is needed to heat the substrate and the thin film, about 0.1 $J\,cm^{-2}$ is due to the $SiO_{0.6}$ film. It is straightforward, that a more evolved nanostructure requires more energy to be formed, i.e. it requires either longer

processing times or higher temperatures. Therefore, since the processing time during laser treatment is much shorter, a higher temperature must have been achieved.

When considering a solid state process, the diffusion constant of O-atoms in the Si-phase rises to $4 \times 10^{-9}\,cm^2\,s^{-1}$ just below the melting point of silicon[49]. This represents an increase by 3 orders of magnitude, not sufficient to explain the observed coarsening of the Si:SiO_2 nanocomposite structure. A further rise in temperature, resulting in a process occurring in the liquid state, leads to a sudden increase of the diffusion of O-atoms in the Si-phase to $3 \times 10^{-4}\,cm^2\,s^{-1}$[49], i.e. by five orders of magnitude. A similar rise upon melting is expected for the diffusion along grain boundaries. This now fully conforms with the experimental findings. We therefore conclude, that during laser treatment, growth and enhanced phase separation occurs in liquid state.

Crystallization during oven treatment is regarded as a classical nucleation and growth process. The observation of many randomly oriented nanocrystals supports the mechanism of nucleation at various places and subsequent growth by heat treatment. During laser processing, vast Si crystallites and an almost full crystallization of the Si-phase were obtained. A thermal process via liquid state leads to a contraction of the Si-phase, since Si has a higher density in the liquid ($2.52\,g/cm^3$[50–52]) than in the solid (crystalline Si:$2.33\,g/cm^3$; amorphous Si:$2.29\,g/cm^3$). SiO_2 on the other hand, expands little during heating[43]. During solidification and cooling, the Si-phase expands, while being confined in the low-expansion material SiO_2. Since the density of crystalline Si is higher compared to the amorphous state, full crystallization is favourable.

The vast Si grains can be explained, in contrast to nucleation and growth, by a process similar to explosive crystallization[53,54]. There, latent heat, released during solidification and crystallization, causes melting of adjacent silicon, resulting in a self-propagating liquid region travelling through the as-deposited amorphous Si:SiO_2 layer. Now, the scanning laser controls the velocity of this process. The crystallization occurs along the moving liquid-solid interface with already crystallized Si acting as seed for the growing crystal grains.

Both, almost full crystallization and vast Si grains support the assumption of a process occurring in the liquid state.

3.3. Formation of interface layers

During thermal treatment, surface and interface layers grow or even evolve. After oven treatment, the initially deposited SiO_2 cover layer more than doubles in thickness. Following laser treatment, the cover layer also grows in size, and additionally silicon-rich interface layers form.

The growth of the cover layer can be explained by further oxidation during thermal treatment. Oven processing was conducted in Ar atmosphere, but residual and effused O_2 from the as-deposited layer, as well as O-atoms from interstitial positions in the Si-phase can still cause oxide formation. Laser treatment was done at normal atmospheric conditions.

Additional Si-rich interface layers observed for laser-treated samples can be explained by the presence of the adjacent silicon oxide surface layer as well as the silica substrate. At first, SiO_2 grows at the interface to these layers, favoured by a lower surface energy of the planar layers compared to SiO_2 nanostructures, leading to an enhanced wetting and preferred growth of the SiO_2 at the substrate and surface oxide layer. For a certain distance to these interface layers, due to the diffusion length of O-atoms during thermal treatment, a volume depleted from oxygen forms. Hence, the formation of a silicon-enriched intermediate layer is caused. In principle, this process should also occur for oven-treated samples. Since diffusion during oven treatment is low compared to laser processing, this effect was not resolved for the treatment process used in this study.

4. Materials and Methods

4.1. Sample deposition and processing

$SiO_{0.6}$ films of 500 nm thickness were prepared by reactive ion beam sputter deposition [55,56] on 20 mm × 20 mm fused silica substrates. An Argon ion beam of 1 keV energy and 35 mA current from a 3 cm Kaufman-type ion source was applied to sputter a 6" silicon target (99.999 %). The ion-source-to-target distance was 18 cm, and the target was tilted by an angle of 22° with respect to the ion beam. The sample was positioned 18 cm away from the target and heated to 450 °C by a boron nitride heater. The base pressure was 2×10^{-5} Pa and the working pressure was 8×10^{-3} Pa. By injection of 1.5 sccm oxygen into the sputtering chamber, that raised the working pressure by 1×10^{-3} Pa, a stoichiometry of $SiO_{0.6}$ was obtained. For protection against post deposition oxidation, a 15 nm SiO_2 top layer was deposited. After cutting the as-deposited sample, a comparative post-deposition treatment was performed by two approaches. Three individual isothermal oven treatments of 90 min at 950 °C with intermediate cooling, all under Ar atmosphere were applied to one part of the sample. The other part was laser-treated at ambient conditions using a 808 nm radiation of an Activation Line 450 diode laser (LIMO) emitting a Gaussian-shaped line focus of 11 mm × 0.1 mm and a power density of 6.4 kW cm^{-2}. A dwell time, assumed to be the full width at half maximum passing by the feed rate of the supposed ideal laser beam, of 17 ms was used.

4.2. Characterization

Elemental composition and depth distribution of the $SiO_{0.6}$ thin films before and after post-deposition treatment were analyzed by RBS using helium ions with an energy of 1.7 MeV from a Van-de-Graaff accelerator. The obtained spectra were fitted with help of the SIMNRA[57] software.

The thin film thicknesses were determined by rotating compensator spectroscopic ellipsometry (SE; M-2000FI from J. A. Woolam Co). The ellipsometric angles Psi and Delta were recorded in the range from 210 nm to 1680 nm at a fixed angle position of 75°. Thickness was obtained by fitting a layer stack model based on reference data for the refractive indices to the measured data. The resulting simulated stack for the as-deposited sample consists of three parts, a fused silica substrate, a bulk layer which was described by a Bruggeman-effective medium approximation (EMA) with different amounts of silicon dioxide[58] and amorphous[32] silicon, and a silicon dioxide top layer. For the annealed samples, Bruggeman EMAs were expanded by adding contributions of crystalline[58] silicon. To validate the obtained thicknesses, selected samples were cross-checked with profilometry using a Veeco DEKTAK 8000 equipped with a 12.5 µm stylus, and punctually by cross-sectional TEM.

Raman spectra were measured with a micro-Raman LabramHR spectrometer (Horiba, France). For excitation, the beam of a frequency-doubled Nd:YAG laser with a wavelength of 532 nm was focused on the samples using a long-working distance objective with 100 fold magnification. The laser power density on the sample was minimized to 3 kW cm^{-2} (0.1 mW laser power) in order to avoid any thermally or photo-induced transformation of Si. The collected Raman-scattered light was dispersed by an 1800 mm^{-1} holographic grating and recorded with a liquid nitrogen cooled CCD detector.

X-ray diffraction was performed with an Empyrean Panalytical Θ-Θ 4-circle diffractometer using the 0.154 nm Cu-Kα line. A parallel beam was established using a parabolic X-ray mirror and a 2 mm fixed mask. An anti-scatter slit of 1.4 mm and a 1/8° fixed divergence slit were used to form the beam incident on the sample at 1°. For the diffracted beam, Soller slits (0.04 rad) and a parallel plate collimator with an opening of 0.27° were used. A proportional Xenon point detector scanned a 2Θ range of 10°-32° and 44°-60° with a step size of 0.05° and a counting time of 80 s per step.

Cross-sectional transmission electron micrographs were obtained using an image C_s-corrected Titan 80-300 (FEI) microscope which is equipped with a Gatan Imaging Filter 863. The primary electrons were accelerated to 300 kV. Additional to high-resolution TEM, energy-filtered TEM (EFTEM) with electrons exhibiting an energy loss of 17 eV due to the excitation of the valence band plasmons

in Si were used for imaging the amorphous and crystalline silicon fractions. Complementary, SiO_2 was imaged using electrons with an energy loss of 27 eV (not shown here). EFTEM analysis was done with a slit width of 5 eV. TEM specimens of as-deposited and oven-treated samples were obtained by classical TEM specimen preparation, i.e. by sawing, grinding, dimpling and final Ar^+ ion milling. For the laser-treated sample, an similar microscope (FEI Tecnai F30) was used for the analysis, and TEM lamella preparation was carried out using a focused ion beam with 30 keV for rough and 5 keV for subtle cutting. The zone of interest was protected by a sputtered 1.5 µm thick layer of platinum.

5. Conclusion

Three-dimensional, percolated Si:SiO_2 networks were obtained by reactive ion beam deposition of thin films with a measured stoichiometry of $SiO_{0.64\pm0.06}$. Subsequent oven and diode line-focused laser treatment led to different degrees of Si crystallization and structural coarsening. For the first time, diode line-laser scanning was applied as thermal treatment to SiO_x films for the creation of Si:SiO_2 nanostructures.

In contrast to predictions and previous studies on percolated Si:SiO_2 networks[7,8,10], phase separation into amorphous silicon and silica occurred during the deposition of $SiO_{0.6}$ layers. During oven treatment, coarsening of the as-deposited structure morphology in a solid state regime occurred by diffusion of O-atoms as well as by grain boundary diffusion. Simultaneously, partial crystallisation of the Si phase by nucleation and growth into nano-sized, randomly oriented crystallites was observed. In contrast, almost perfectly, fully crystalline Si and further coarsened structures were obtained by laser processing for considerable shorter treatment times. The larger structures were associated with a much higher temperature achieved during millisecond laser processing, eventually occurring in the liquid state of silicon, and resulting in a orders of magnitude higher diffusion constant. Perfect crystallinity resulted from the higher density of crystalline silicon, since the volume of the expanding silicon phase was restricted during solidification by the silica matrix. The vast extension of the obtained Si crystal grains resulted from crystallization along the liquid-solid interface during a process similar to explosive crystallization. In-plane tensile and out-of-plane compressive strain was explained by different thermal contraction, during cooling in the solid, of the fused silica substrate and the Si phase inside the Si:SiO_2 layer. The growth of interface layers was favoured by the lower surface energy of the planar surface silica and fused silica substrate compared to nanostructures of SiO_2. The oxygen depletion and therefore silicon enrichment of the $SiO_{0.6}$ layer in the vicinity of these silica interfaces led to the formation of Si interlayer for laser treated films.

The study demonstrates the high potential of diode line-laser scanning to form percolated Si:SiO_2 nanocomposites, and shows on the other hand that different thermal treatments are required to cover the whole structure size scale of nano-silicon.

Author Contributions: E.S. designed and conducted thin film deposition, thermal processing, RBS incl. analysis, SE incl. analysis and Raman spectroscopy. R.H. conducted and analysed TEM investigations, J.G. measured and analysed XRD. M.K. analysed Raman spectroscopy. E.S. and M.K. wrote the manuscript. Supervision, Reviewing and Funding Acquisition was done by S.G. and M.K. . All authors approved the final version of the manuscript.

Funding: This work has received funding from the European Union's Horizon 2020 research and innovation programme under the Marie Skłodowska-Curie grant agreement No 645725. S.G. gratefully acknowledges funding by the Initiative and Networking Funds of the Helmholtz Association through the W3 programme.

Acknowledgments: Support by the Ion Beam Center (IBC) and IBC structural characterization facilities at HZDR is gratefully acknowledged. Special thank by the authors is addressed to Verónica Carcelen Valero and Abengoa Research (Seville, Spain) for selected EFTEM imaging; G. Schnabel, M. Missbach, A. Kunz, A. Schneider, A. Scholz, J. Zscharschuch (all from HZDR) for technical assistance, and F. Lungwitz, R. Wenisch, D. Janke, Karl-Heinz Heinig and A. Erbe (all from HZDR) for helpful discussions and careful proofreading of the manuscript.

Conflicts of Interest: The authors declare no conflict of interest. The founding sponsors had no role in the design of the study; in the collection, analyses, or interpretation of data; in the writing of the manuscript, and in the decision to publish the results.

1. Bardeen, J.; Brattain, W.H. The Transistor, A Semiconductor Triode. *Physical Review* **1948**, *74*, 230–231. doi:10.1109/JPROC.1998.658753.
2. Shockley, W. The Theory of p-n Junctions in Semiconductors and p-n Junction Transistors. *Bell System Technical Journal* **1949**, *28*, 435–489. doi:10.1002/j.1538-7305.1949.tb03645.x.
3. Tanenbaum, M.; Thomas, D.E. Diffused Emitter and Base Silicon Transistors. *Bell System Technical Journal* **1956**, *35*, 1–22. doi:10.1002/j.1538-7305.1956.tb02371.x.
4. Priolo, F.; Gregorkiewicz, T.; Galli, M.; Krauss, T.F. Silicon nanostructures for photonics and photovoltaics. *Nature nanotechnology* **2014**, *9*, 19–32. doi:10.1038/nnano.2013.271.
5. Szczech, J.R.; Jin, S. Nanostructured silicon for high capacity lithium battery anodes. *Energy & Environmental Science* **2011**, *4*, 56. doi:10.1039/c0ee00281j.
6. Heitmann, J.; Müller, F.; Zacharias, M.; Gösele, U. Silicon nanocrystals: size matters. *Advanced Materials* **2005**, *17*, 795–803. doi:10.1002/adma.200401126.
7. Müller, T.; Heinig, K.H.; Möller, W. Size and location control of Si nanocrystals at ion beam synthesis in thin SiO2 films. *Applied Physics Letters* **2002**, *81*, 3049–3051, [arXiv:cond-mat/0208137]. doi:10.1063/1.1512952.
8. Liedke, B.; Heinig, K.H.; Mücklich, A.; Schmidt, B. Formation and coarsening of sponge-like Si-SiO2 nanocomposites. *Applied Physics Letters* **2013**, *103*, 133106. doi:10.1063/1.4822125.
9. Keleş, Ü.; Liedke, B.; Heinig, K.H.; Bulutay, C. Networks of silicon nanowires: A large-scale atomistic electronic structure analysis. *Applied Physics Letters* **2013**, *103*, 203103. doi:10.1063/1.4830039.
10. Friedrich, D.; Schmidt, B.; Heinig, K.H.; Liedke, B.; Mücklich, a.; Hübner, R.; Wolf, D.; Kölling, S.; Mikolajick, T. Sponge-like Si-SiO2 nanocomposite - Morphology studies of spinodally decomposed silicon-rich oxide. *Applied Physics Letters* **2013**, *103*, 131911. doi:10.1063/1.4820453.
11. Ilday, S.; Ilday, F.Ö.; Hübner, R.; Prosa, T.J.; Martin, I.; Nogay, G.; Kabacelik, I.; Mics, Z.; Bonn, M.; Turchinovich, D.; Toffoli, H.; Toffoli, D.; Friedrich, D.; Schmidt, B.; Heinig, K.H.; Turan, R. Multiscale Self-Assembly of Silicon Quantum Dots into an Anisotropic Three-Dimensional Random Network. *Nano Letters* **2016**, *16*, 1942–1948. doi:10.1021/acs.nanolett.5b05158.
12. Gundogdu, S.; Ozen, E.S.; Hübner, R.; Heinig, K.H.; Aydinli, A. Laser induced sponge-like Si in Si-rich oxides for photovoltaics. *Optics Express* **2013**, *21*, 24368–74. doi:10.1364/OE.21.024368.
13. Nastasi. *Ion solid interactions*; Cambrige, 1996.
14. Möller, W. WTB-HZDR-073: Fundamentals of ion-solid interaction - a compact introduction. Technical report, Helmholtz-Zentrum Dresden - Rossendorf, Dresden, 2016.
15. Houben M. Luysberg P. Hapke R. Cari, L. Structural properties of microcrystalline silicon in the transition from highly crystalline to amorphous growth. *Philosophical Magazine A* **1998**, *77*, 1447–1460. doi:10.1080/014186198253840.
16. Ossadnik, C.; Vepřek, S.; Gregora, I. Applicability of Raman scattering for the characterization of nanocrystalline silicon. *Thin Solid Films* **1999**, *337*, 148–151. doi:http://dx.doi.org/10.1016/S0040-6090(98)01175-4.
17. Russell, J.P. Raman scattering in silicon. *Applied Physics Letters* **1965**, *6*, 223–224. doi:10.1063/1.1754144.
18. Parker Jr., J.H.; Feldman, D.W.; Ashkin, M. Raman scattering by silicon and germanium. *Physical Review* **1967**, *155*, 712. doi:10.1103/PhysRev.155.712.
19. Smith, J.E.; Brodsky, M.H.; Crowder, B.L.; Nathan, M.I.; Pinczuk, A. Raman spectra of amorphous Si and related tetrahedrally bonded semiconductors. *Physical Review Letters* **1971**, *26*, 642–646. doi:10.1103/PhysRevLett.26.642.
20. Bermejo, D.; Cardona, M. Raman scattering in pure and hydrogenated amorphous germanium and silicon. *Journal of Non-Crystalline Solids* **1979**, *32*, 405–419. doi:https://doi.org/10.1016/0022-3093(79)90085-1.
21. Wolf, I.D.; Jiménez, J.; Landesman, J. Raman and luminescence spectroscopy for microelectronics. *Catalogue of optical and ...* **1998**.
22. Iqbal, Z.; Vepřek, S. Raman scattering from hydrogenated microcrystalline and amorphous silicon. *J. Phys. C: Solid State Physics* **1982**, *15*, 377–392. doi:doi:10.1088/0022-3719/15/2/019.
23. Iqbal, Z.; Vepřek, S.; Webb, A.; Capezzuto, P. Raman scattering from small particle size polycrystalline silicon. *Solid State Communications* **1981**, *37*, 993–996. doi:10.1016/0038-1098(81)91202-3.

24. Smit, C.; van Swaaij, R.; Donker, H.; Petit, A.; Kessels, W.; van de Sanden, M. Determining the material structure of microcrystalline silicon from Raman spectra. *JOURNAL OF APPLIED PHYSICS* **2003**, *94*, 3582–3588. doi:{10.1063/1.1596364}.
25. Richter, H.; Wang, Z.P.; Ley, L. The one phonon Raman spectrum in microcrystalline silicon. *Solid State Communications* **1981**, *39*, 625–629. doi:10.1016/0038-1098(81)90337-9.
26. Hart, T.; Aggarwal, R.; Lax, B. Temperature Dependence of Raman Scattering in Silicon. *Physical Review B* **1970**, *1*, 638–642. doi:10.1103/PhysRevB.1.638.
27. Kobliska, R.J.; Solin, S.A. Raman spectrum of wurtzite silicon. *Physical Review B* **1973**, *8*, 3799–3802. doi:10.1103/PhysRevB.8.3799.
28. i Morral, A.; Arbiol, J.; Prades, J.D.; Cirera, A.; Morante, J.R. Synthesis of Silicon Nanowires with Wurtzite Crystalline Structure by Using Standard Chemical Vapor Deposition. *Advanced Materials* **2007**, *19*, 1347–1351. doi:10.1002/adma.200602318.
29. XIA, H.; HE, Y.; WANG, L.; ZHANG, W.; LIU, X.; ZHANG, X.; FENG, D.; JACKSON, H. PHONON MODE STUDY OF SI NANOCRYSTALS USING MICRO-RAMAN SPECTROSCOPY. *JOURNAL OF APPLIED PHYSICS* **1995**, *78*, 6705–6708. doi:{10.1063/1.360494}.
30. Bustarret, E.; Hachicha, M.a.; Brunel, M. Experimental determination of the nanocrystalline volume fraction in silicon thin films from Raman spectroscopy. *Applied Physics Letters* **1988**, *52*, 1675–1677. doi:10.1063/1.99054.
31. Tsu, R.; Gonzalez-Hernandez, J.; Chao, S.S.; Lee, S.C.; Tanaka, K. Critical volume fraction of crystallinity for conductivity percolation in phosphorus-doped Si:F:H alloys. *Applied Physics Letters* **1982**, *40*, 534–535. doi:10.1063/1.93133.
32. Palik, E. *Handbook of Optical Constants of Solids*; Academic Press, 1997. doi:10.1016/B978-012544415-6.50143-6.
33. Vella, E.; Messina, F.; Cannas, M.; Boscaino, R. Unraveling exciton dynamics in amorphous silicon dioxide: Interpretation of the optical features from 8 to 11 eV. *Physical Review B - Condensed Matter and Materials Physics* **2011**, *83*, 4–11, [1009.3873v1]. doi:10.1103/PhysRevB.83.174201.
34. Morris, M.C.; McMurdie, H.F.; Evans, E.H.; Paretzkin, B.; de Groot, J.H.; Hubbard, C.R.; Carmel, S.J. Standard x-ray diffraction powder patterns: - 13- data for 58 substances. In *Standard x-ray diffraction powder patterns*; National Bureau of Standards (US): Wahingron. D.C., 1976; Vol. 13, p. 114. doi:10.6028/NBS.MONO.25-13.
35. Williamson, G.; Hall, W. X-ray line broadening from filed aluminium and wolfram. *Acta Metallurgica* **1953**, *1*, 22–31. doi:10.1016/0001-6160(53)90006-6.
36. de Wolf, I. Micro-Raman spectroscopy to study local mechanical stress in silicon integrated circuits. *Semiconductor Science and Technology* **1996**, *11*, 139–154.
37. Paillard, V.; Puech, P.; Sirvin, R.; Hamma, S.; Roca i Cabarrocas, P. Measurement of the in-depth stress profile in hydrogenated microcrystalline silicon thin films using Raman spectrometry. *Journal of Applied Physics* **2001**, *90*, 3276. doi:10.1063/1.1396828.
38. Faraci, G.; Gibilisco, S.; Pennisi, A.R.; Faraci, C. Quantum size effects in Raman spectra of Si nanocrystals. *Journal of Applied Physics* **2011**, *109*, 074311. doi:10.1063/1.3567908.
39. Duan, Y.; Kong, J.F.; Shen, W.Z. Raman investigation of silicon nanocrystals: quantum confinement and laser-induced thermal effects. *Journal of Raman Spectroscopy* **2012**, *43*, 756–760. doi:10.1002/jrs.3094.
40. Kleovoulou, K.; Kelires, P.C. Stress state of embedded Si nanocrystals. *Physical Review B* **2013**, *88*, 085424. doi:10.1103/PhysRevB.88.085424.
41. Anastassakis, E.; Pinczuk, A.; Burstein, E. Effect of static uniaxial stress on the Raman spectrum of silicon. *Solid State Communications* **1970**, *8*, 133–138.
42. Hopcroft, M.a.; Nix, W.D.; Kenny, T.W. What is the Young ' s Modulus of Silicon ? *Journal of Microelctromechanical Systems* **2010**, *19*, 229–238. doi:10.1109/JMEMS.2009.2039697.
43. Souder, W.; Hidnert, P. Measurements on the Thermal Expansion of Fused Silica. *Scientific papers of the bureau of standards* **1925**, *21*, 1–23.
44. Okaji, M. Absolute thermal expansion measurements of single-crystal silicon in the range 300-1300 K with an interferometric dilatometer. *International Journal of Thermophysics* **1988**, *9*, 1101–1109. doi:10.1007/BF01133277.

45. Tada, H.; Kumpel, a.E.; Lathrop, R.E.; Slanina, J.B.; Nieva, P.; Zavracky, P.; Miaoulis, I.N.; Wong, P.Y. Thermal expansion coefficient of polycrystalline silicon and silicon dioxide thin films at high temperatures. *Journal of Applied Physics* **2000**, *87*, 4189–4193. doi:10.1063/1.373050.
46. Tsoukalas, D.; Tsamis, C.; Normand, P. Diffusivity measurements of silicon in silicon dioxide layers using isotopically pure material. *Journal of Applied Physics* **2001**, *89*, 7809. doi:10.1063/1.1371003.
47. Mehrer, H. *Diffusion in Solids*; Springer-Verlag Berlin Heidelberg, 2007.
48. Herzig, C.; Mishin, Y. *Grain-Boundary Diffusion in Metals*; Springer,: Berlin Heidelberg, 2005.
49. Tang, K.; Øvrelid, E.J.; Tranell, G.; Tangstad, M. Critical assessment of the impurity diffusivities in solid and liquid silicon. *JOM* **2009**, *61*, 49–55.
50. Sasaki, H.; Tokizaki, E.; Terashima, K.; Kimura, S. Density Variation of Molten Silicon Measured by an Improved Archimedian Method. *Japanese Journal of Applied Physics* **1994**, *33*, 3803–3807.
51. Nakanishi, H.; Nakazato, K.; Abe, K.; Maeda, S.; Terashima, K. Temperature dependence of the density of molten germanium and silicon measured by a newly developed Archimedian technique. *Journal of Crystal Growth* **1999**, *203*, 75–79. doi:10.1016/S0022-0248(99)00089-5.
52. Endo, R.K.; Fujihara, Y.; Susa, M. Calculation of the density and heat capacity of silicon by molecular dynamics simulation. *http://www.thermophysics.ru*. doi:10.1068/htjr135.
53. Thompson, M.; Galvin, G.; Mayer, J. Melting temperature and explosive crystallization of amorphous silicon during pulsed laser irradiation. *Physical review letters* **1984**, *52*, 2360–2364. doi:10.1103/PhysRevLett.52.2360.
54. Geiler, H.D.; Glaser, E.; Götz, G.; Wagner, M. Explosive crystallization in silicon. *Journal of Applied Physics* **1986**, *59*, 3091–3099. doi:10.1063/1.336910.
55. Abrasonis, G.; Krause, M.; Mücklich, A.; Sedlačková, K.; Radnóczi, G.; Kreissig, U.; Kolitsch, A.; Möller, W. Growth regimes and metal enhanced 6-fold ring clustering of carbon in carbon–nickel composite thin films. *Carbon* **2007**, *45*, 2995–3006. doi:10.1016/j.carbon.2007.09.044.
56. Krause, M.; Buljan, M.; Mücklich, A.; Möller, W.; Fritzsche, M.; Facsko, S.; Heller, R.; Zschornak, M.; Wintz, S.; Endrino, J.L.; Baehtz, C.; Shalimov, A.; Gemming, S.; Abrasonis, G. Compositionally modulated ripples during composite film growth: Three-dimensional pattern formation at the nanoscale. *Physical Review B - Condensed Matter and Materials Physics* **2014**, *89*, 1–9. doi:10.1103/PhysRevB.89.085418.
57. Mayer, M. SIMNRA, 2006.
58. Herzinger, C.M.; Johs, B.; Mcgahan, W.a.; Woollam, J.a.; Paulson, W. Ellipsometric determination of optical constants for silicon and thermally grown silicon dioxide via a multi-sample , multi-wavelength , multi-angle investigation. *Journal of Applied Physics* **1998**, *83*, 3323–3336. doi:10.1063/1.367101.